New nanocrystalline manganese oxides as cathode materials for lithium batteries : electron microscopy, electrochemical and X-ray absorption studies

Pierre Strobel, Céline Darie, François Thiéry, Maria Bacia, Olivier Proux, Alejandro Ibarra-Palos, Jean-Bruno Soupart

New nanocrystalline manganese oxides as cathode materials for lithium batteries : electron microscopy, electrochemical and X-ray absorption studies

P. Strobel[1], C. Darie[1], F. Thiéry[1], M. Bacia[1], O. Proux[2], A. Ibarra-Palos[1]* and J.B. Soupart[3]*

[1] Centre National de la Recherche Scientifique, Laboratorire de Cristallographie, BP166, 38042 Grenoble Cedex 9, France

[2] Laboratoire de Géophysique Interne et Tectonophysique, UMR CNRS - Université Joseph Fourier, 1381, rue de la Piscine, 38400 Saint-Martin-d'Hères, France

[3] Erachem-Comilog, B-7333 Tertre, Belgium

* Now at Instituto de Investigaciones en Materiales, Universidad Nacional Autónoma de México, A.P. 70-360, Ciudad Universitaria, Coyoacan 04510, México, D.F.

Abstract

New nanostructured manganese oxi-iodides were prepared by redox reaction of sodium permanganate with lithium iodide in aqueous medium at room temperature. Transmission electron microscopy (TEM) showed that they are nanocrystalline with grain size in the 5-10 nm range. TEM and X-ray absorption confirmed the short-range orderded structure of these compounds, which contain octahedrally coordinated manganese atoms. The electrochemical properties were studied as a function of preparation conditions (Li/Mn ratio, carbon incorporation at the synthesis stage and grinding). Best electrochemical results were obtained either on samples with carbon black incorporated directly in the aqueous reaction medium at the synthesis stage, or on samples with carbon mixed after synthesized, submitted to extensive grinding. Typical capacities in the potential window 1.8-3.8 V are160 and 130 mAh/g at the 40th and 100th cycle, respectively. Step-potential electrochemical spectroscopy and the evolution of X-ray absorption spectra on discharge are consistent with a single-phase lithium intercalation reaction with simultaneous manganese oxidation-reduction.

Keywords: manganese oxide, lithium batteries, nanomaterials

Corresponding author:

Pierre Strobel, tel. 33 476 887 940, fax 33 476 881 038, email: strobel@grenoble.cnrs.fr

Introduction

Good electrode materials for lithium batteries are actively sought among oxides of transition elements meeting following requirements : (1) several accessible oxidation states giving adequate potentials (mainly V, Mn, Co, Ni, and Fe in some oxoanionic compounds), (2) open structures permitting topotactic insertion/extraction reactions with lithium. In practical tests, however, many of these materials remain far from their theoretical lithium insertion capacities. Major factors for this are the instability of fully deintercalated materials (for instance Li_xCoO_2 or Li_xNiO_2 at low x value), but also the low electronic conductivity of most transition oxides.

The conductivity problem can be partly circumvented by including a conducting additive (usually carbon) in the electrode paste, and has given rise to interesting experimental advances in the fabrication of carbon composites with manganese oxides [1,2], and especially with the very promising, but highly insulating $LiFePO_4$ cathode material [3,4]. In this perspective, the state of division of the insertion host oxide can be expected to play a significant role. Indeed, Kang and Goodenough showed that in the well-known Li-Mn-O spinel system, capacity fading for the $LiMn_2O_4$ ™ $Li_2Mn_2O_4$ reaction could be mostly suppressed by extended milling, giving rise to an important decrease in particle size [5,6]. Numerous works regarding the influence of particle size on electrochemical insertion properties of oxides appeared in the last five years [7-12]. The decrease of particle size led to sub-micrometric powders ; in manganese oxide systems, several studies of such products as cathode materials were reported [13-16].

The next breakthrough, however, came from a more drastic synthetic approach, namely the preparation of X-ray-amorphous oxides. The reaction of permanganate ion with various reducing agents has been known for decades to yield mostly layered manganates [17-20]. In 1997, Kim and Manthiram [21] reported remarkable electrochemical capacity for an oxi-iodide prepared by the reaction of sodium permanganate with lithium iodide in non-aqueous medium. More recently [22], Ibarra-Palos et al. showed that X-ray amorphous products could be obtained by reacting sodium permanganate with various reducing agents in aqueous medium (Cl^-, I^-, hydrogen peroxide, oxalic acid), The iodide route gave the best product in terms of ease of dehydration and electrochemical performances.

In this paper, we report a more detailed study of products of the NaMnO4–LiI reaction in aqueous medium. In the absence of usable information from X-ray diffraction, structural

characterization tools used are transmission electron microscopy (TEM) and X-ray absorption (XAS). The former is invaluable to ascertain whether a given sample is actually amorphous or crystallized at the nanometer scale; to our knowledge this is the first report of such a study in X-ray amorphous manganese oxi-iodides. XAS allows to probe the local environment of an absorbing element (here manganese) and to follow the variation of its environment and oxidation state with lithium insertion. It has been recently used in the study of nanometric or amorphous manganese oxides by several groups [23-26].

These materials were tested in lithium electrochemical cells in both galvanostatic and potentiostatic mode. The importance of the quality of mixing with conducting carbon (ensured by two different experimental procedures) will be stressed. Samples with remarkable stability on cycling (ca. 130 mAh/g after 100 cycles) were obtained by optimizing these factors. A preliminary report of electrochemical measurements appeared elsewhere [27].

Experimental

Synthesis procedure. – The starting reagents were NaMnO4 and LiI (Aldrich). All reactions were carried out at room temperature in at least a 6-fold excess Li^+ (aqueous LiI solution) with respect to $NaMnO_4$ concentration. A 0.5 M aqueous solution of sodium permanganate was first prepared, then an appropriate amount of a 1.5 M aqueous solution of LiI was added. The mixture was vigorously stirred for 15 hours. In the case of samples including carbon black at the synthesis stage, 250 mg of carbon black (Y50A grade, SNNA, Berre, France) was added to the LiI solution under stirring. Products were washed with distilled water, filtered and dried at 80°C in air.

For the study of the effect of particle division, samples were ground using a rotary mixer/grinder Retsch RM 100 where mixtures were subjected to grinding at 200 rpm for various durations between 15 and 60 minutes.

Chemical and structural characterization. – Samples were studied by X-ray diffraction (XRD) using a Siemens D-5000 diffractometer with Cu Kα radiation. The morphology and iodine/manganese ratio were determined using a JEOL 840 scanning electron microscopy equipped with coupled EDX spectroscopic analysis. Li, Na and Mn contents were measured by atomic absorption spectrophotometry. The manganese oxidation state was determined by standard oxalate/permanganate volumetric titration after dissolution of samples in 2M

sulphuric acid. Iodine/manganese ratios were obtained from EDX. Transmission electron microscopy was carried out using a Philips CM300 microscope operated at 300 kV (resolution 1.9 Å). Samples for TEM observation were ground under acetone and deposited on copper grids covered with thin holey carbon films.

Electrochemical measurements. – Electrochemical tests were carried out in liquid electrolyte at room temperature using Swagelok-type batteries at room temperature. Cathodic paste were prepared by intimately mixing the oxide powder with carbon black (for those samples where carbon was not added earlier) and PTFE emulsion in weight ratio 70:20:10. This paste was rolled down to 0.1 mm thickness, cut into pellets with diameter 10 mm and dried at 240°C under vacuum. Typical active material weights used were 6-12 mg/cm^2. The electrolyte was a 1 M solution of $LiPF_6$ in EC-DMC 1:2. Negative electrodes were 200 µm-thick lithium foil (Metall Ges., Germany). Cells were assembled in a glove box under argon with ≤ 1 ppm H_2O. Electrochemical studies were carried out using a MacPile Controller (Bio-Logic, Claix, France) in the potential window 1,8-3,8 V, in either galvanostatic mode or by step-potential electrochemical spectroscopy (SPES) [28], using typically 10 mV/30mn steps.

X-ray absorption spectroscopy. – X-ray Absorption Spectroscopy experiments were performed at the CRG-FAME beamline (BM30B) at the European Synchrotron Radiation Facility storage ring in Grenoble, operating in 16 bunchs mode at 6 GeV [29]. Spectra were recorded in transmission mode at the Mn K edge, using a double-crystal Si(220) monochromator. The intensities of the incident and transmitted beams were measured using Si diodes. The full fan delivered by the bending magnet source was focused in the horizontal plane by the second crystal of the monochromator and by the second Rh-coated mirror in the vertical plane. Finally, a feedback system was used to maximize the output of the two-crystal X-ray monochromator. The size of the X-ray spot, around 300 x 200 µm^2 (HxV FWHM), and its position on the sample were kept constant during the acquisition.

Samples for XAS measurements were pellets of diameter 10 mm made of the oxide diluted in boron nitride in appropriate proportions to give an optimum absorption jump. For the sample studied after electrochemical discharge, the thickness of the electrode pellet was adjusted to give the appropriate absorption and used as is on the beamline after opening the battery. The absolute energy scale was calibrated using a Mn metal sheet. The energy calibration was initially performed with a Mn metal foil (E_K=6.539keV) and carefully

checked for each spectrum by measuring the absorption of the metallic reference, using the transmitted beam threw the samples as an incident beam for the pure Mn foil.

The oxidation state of manganese was estimated by comparing the near-edge features (XANES) with following reference compounds : $LiMn_2O_4$ [30], λ-MnO_2 (prepared by chemical extraction of lithium from $LiMn_2O_4$), and Mn_2O_3 (prepared by heating MnO_2 at 750°C in air for 24 hours). λ-MnO_2 was used as a Mn^{4+} standard because it has 6 equal Mn–O distances, whereas the more common form β-MnO_2 with rutile-type structure has 4 short + 2 longer Mn–O distances.

EXAFS oscillations χ(k) were extracted from the raw data using the Athena program [31]. All the analysis were performed with the $k^2\chi(k)$ signals. The Fourier Transform (FT) of the $k^2\chi(k)$ signal was performed over the 2.6 – 11.9 Å k-range to obtain the so-called radial distribution pseudo-function, which displays peaks roughly characteristic of each shell around the central Mn atoms. Filtering of the first two peaks in the FT (containing the contribution of Mn–O and/or Mn–Mn shells) was done by inverse FT over the 0.6 – 2.9 Å R-range with a Kaiser window $\tau = 2.5$. The fitting procedure was performed on the filtered $k^2\chi(k)$ signals with the Artemis program [31].

Results and discussion

1. Synthesis and composition

Table I summarizes the preparation conditions and composition of samples obtained. All products have an alkali metal/Mn ratio in the range 0.53-0.63. Samples B–D are very close in composition, with low levels of residual sodium (Na/Mn ≤ 0.08). In all cases, the total alkali cation contents are much lower than those reported for syntheses in non-aqueous medium [ref. Kim]. The oxidation state determination gave results in excess of Mn^{4+}, which can be explained by the contribution of iodine. Hwang et al. [32] recently showed that iodine species in such manganese 'oxy-iodides' prepared in aqueous medium are most likely iodate anions IO_3^-. These obviously participate in the redox titration, where their contribution cannot be separated from that of manganese. The iodine fraction was determined with limited accuracy (see Table I); however, a combination of the total oxidizing power and iodine concentration yields manganese valence close to 4 in all samples.

Finally, we note that the inclusion of 250 mg carbon black in the reaction medium (for samples B and D) resulted in a large C/Mn molar ratio (in the 1.6-1,7 range) in the

precipitates.

2. Physico-chemical characterization

Figure 1 shows the XRD patterns of as-prepared samples. All products exhibit similar features in diffraction, i.e. the absence of any significant peaks, indicating either an amorphous character or a very short coherence length corresponding to very small crystallites. The inclusion of carbon black during synthesis and the variation in Li/Mn ratio did not significantly change the XRD patterns.

The measurement of specific surface area yielded values of 20 and 46 m^2/g for samples A and C, respectively.

The grain size and homogeneity of cathodic films for battery electrodes, as well as the effect of grinding, has been checked by scanning electron microscopy. Figure 2 shows micrographs of samples C and D at low magnification. Pristine sample A is rather heterogeneous and contains particles up to 50-100 μm, obviously resulting in a rather poor contact with the carbon additive and binder (Figure 2a). Figures 2b and c show the improvement brought in by grinding, with the breaking up of the largest grains and better homogeneity. On the other hand, sample D prepared with carbon included at the synthesis stage is initially much more homogeneous, and shows little difference before and after grinding (Figure 2d and e). The same trends are observed on samples A and B, which are shown in Figure 3 at higher magnification : a considerable increase of homogeneity for sample A, while sample B (with carbon included at the synthesis stage) is practically unchanged by grinding. It seems that the incorporation of carbon black in the reaction medium not only ensures the presence of carbon finely divided in the precipitated oxide, but also favors a smaller particle size and higher homogeneity of the oxide. Note that the carbon content in samples B and D is rather high : C/Mn (atomic) ≈ 1.7 (see table 1), meaning an even larger fraction of carbon in volume.

3. Transmission electron microscopy

More morphological and structural details were revealed by high-resolution transmission electron microscopy. The actual crystallite size is very small : Figure 4 shows that grains of samples A and D have both edge lengths in the 5-10 nm range. At higher magnification, these materials give fringes (Fig.4c) and diffraction rings - albeit broad (Fig.5), indicating that these materials are not amorphous, but are at least partially ordered at the nanometric scale. The

main measurable d-spacings observed are 2.50 ± 0.02 and 2.05 ± 0.02 Å, which correspond to classical interreticular distances found in most structures built up from octahedral Mn^{+4}-O arrangements (311 and 004 planes in spinel, 101 and 111 planes in rutile, 100 and 101 in hexagonal epsilon-MnO_2, respectively [33]).

4. Electrochemical behaviour

Step-potential cyclings at slow rate (10 mV/30 mn) show a unique, broad current peak with maximum around 2.7 V in discharge and 3.5 V in charge (Fig. 6a). An detailed examination of the current evolution during incremental potential steps (fig. 6b) shows that this phenomenon is diffusion-controlled throughout the reduction peak. This and the significant overlap between reduction and oxidation peaks indicate that the lithium insertion/extraction process occurs in a single-phase mechanism

The corresponding discharge-charge curves are smooth, S-shaped curves (see Fig. 7). This behaviour was common to samples A-D, and agrees well with other studies on amorphous or nanometric manganese oxides [22, 34-35]. The charge-discharge curve shape does not change significantly on cycling, and differs considerably from the behaviour of long-range 2D or 3D manganese oxide networks such as spinel or $LiMnO_2$. No evidence of conversion to spinel was found, unlike in the case of crystallised birnessites [36,37].

Figure 7 also shows that the quality of oxide-carbon mixing has a significant effect on capacity. Samples B and D, for which carbon was included at the synthesis stage, have first cycle capacities in excess of 150 mAh/g, whereas the 2.7 V plateau is interrupted much earlier with cathodes made by simple mechanical mixing of oxide and carbon after synthesis (samples A and C). In the latter samples, we also note that the voltage increase during relaxation at the end of discharge is much larger : the cell potential goes back up to 2.5 V for both A and C within 3 hours, compared to 2.07 V for samples B and D. This feature shows that the mixture with carbon mixed after synthesis is unsatisfactory, and that the reduction process during discharge in samples A and C is probably hindered by bad intergrain conduction, leaving a significant fraction of the positive electrode unused.

In order to improve the conductivity and intergrain contact in the cathode, samples were ground for different durations (0, 15 or 60 mn) at 200 rpm. The effect of this treatment is shown in Figure 8. For samples with carbon mechanically mixed after synthesis (Fig. 8a), grinding increases significantly the capacity, whereas the opposite effect is observed in samples with carbon added at the synthesis stage (Fig. 8b),

The effect of grinding on electrochemical performances can be explained as follows. As already shown by the limited discharge plateau length and high voltage change on relaxation at end of discharge, the capacity of samples with carbon added by post-synthesis mixing is rather poor due to bad oxide-carbon grain contact. Grinding reduces the grain size and improves the contact between oxide and carbon grains, thereby increasing the available electrochemical capacity. In samples with carbon included at the synthesis stage, on the contrary, grains are much smaller and the contact between oxide and carbon grains much more intimate. In this case, the grain size is not improved by grinding and we suspect that grinding shocks partially break the oxide-carbon contacts.

Electrochemical capacity and cycling stability. – All samples were cycled for extended durations at C/10-C/20 rate. As shown in Fig. 9, the capacity is rather stable or shows a light decrease with cycle number. Note that the average capacity is not observed at the first discharge. We attribute this to the fact that the valence of Mn is lower than 4 in the initial material, and that the presence of lithium in the initial material makes it possible to push the lithium extraction on charge to a higher valence and lower lithium content than in the initial material. For instance in sample C, assuming a manganese valence of 3.9 :

– 1st. discharge (lithium intercalation):

$$Li_{0.53}Na_{0.06}Mn^{+3.9}O_x + 0.9\ Li\ (\text{theoretical limit}) \rightarrow Li_{1.43}Na_{0.06}Mn^{+3.0}O_x$$

– 1st. charge (lithium deintercalation):

$$Li_{1.43}Na_{0.06}Mn^{+3.0}O_x \rightarrow Li_{0.43}Na_{0.06}Mn^{+4.0}O_x + Li$$

yielding capacities Δx of 0.9 and 1.0 Li on discharge and charge, respectively. This effect is rather significant ; it is clearly visible for all battery cyclings shown in Figure 9, and results in capacity increases in the range 12-15 % between the first and second discharges.

Figure 9 also allows to compare the cycling performances as a function of cathode grinding. The trend observed in the first discharge is maintained, i.e. capacity is improved by grinding for samples with carbon mechanically added after synthesis (sample C), and slightly decreased for samples with carbon added at the synthesis stage (D). A plot of capacity vs. grinding time (Figure 10) shows that this effect is quite spectacular on sample C, even after 15 mn grinding. At the 30ieth cycle, for instance, the capacity of pristine (non-ground) sample C is only 72 % of that of sample D cycled in similar conditions, whereas it increases to 108 % after 60 mn grinding. In summary, the initial capacity and cycling performance are both optimized either by including carbon black in the synthesis stage, or by grinding of

cathode material in the case of mechanical mixing with carbon after synthesis.

Figure 11 shows the capacity up to 100 cycles for optimized materials (sample C - ground and sample D, not ground). The capacities remain high (160 mAh/g) up to ca. 40 cycles, and decrease slowly but constantly on further cycling. It is, however, higher than that of manganese spinels, which behave very poorly in the same potential range (1.8-3.8 V used here). We believe that this decrease is mostly due to inter-grain conductivity problems, and that it could be reduced by specific coating [38] or further carbon mixing optimization processes.

Effect of chemical composition. – Table 1 shows that we also attempted to vary the composition of the reaction medium and hence of the material obtained. The trends outlined above distinguished only two sets so far : samples with carbon added at the synthesis stage (B and D) and samples with carbon mixed later (A and C). A more detailed analysis of the capacity values gives results shown as histograms in Figure 12. In both sets, the sample with higher Li/Mn ratio and higher iodine content (C and D in Table I) systematically yielded better cycling performances. It should be pointed out that the iodine content could not be increased further ; a synthesis aiming at a higher iodine content actually gave worse capacity results ; other studies also concluded to a very limited concentration range of iodine in such oxides [39].

5. X-Ray absorption analysis

EXAFS spectra were recorded on samples giving the best electrochemical performances, i.e. sample C with 60 mn grinding and sample D, as well as on a cathodic pellet recovered from a lithium battery after discharge of sample C.

The near-edge spectra (XANES) are shown in Figure 13, including also the spectra of standards : λ-MnO_2, $LiMn_2O_4$ and Mn_2O_3, with manganese valences 3.98, 3.50 and 3.00, respectively. The spectra for samples C and D are almost superimposable, indicating a very similar manganese local structure and valence in both compounds. The edge position is known to vary with the oxidation state (OS) of the absorber, with the edge shifted towards higher energies with increasing valence [40]. Figure 13 shows that our data indeed follow this trend : λ-MnO_2 and the pristine samples C and D have the highest peak maximum energy, followed (in order of decreasing energy) by $LiMn_2O_4$, sample C after discharge, and Mn_2O_3. These data are plotted quantitatively in Figure 14, showing that (1) the manganese OS in

samples C and D is close to +3.95, (2) the variation of oxidation state with discharge is consistent with a lithium insertion mechanism (giving $\Delta OS = 0.60$ for the battery used).

All spectra also show a small pre-edge double peak (in the 6540-6545 eV range). This feature is associated to 1s→3d transitions, the strength of which depends on the absorber' site symmetry [41,42]. The experimental spectra of samples C and D are very similar to those of the standards in this region, and are consistent with an octahedral or near-octahedral coordination of manganese in all samples.

Regarding EXAFS, fits were performed after filtering in the r-space range 0.7 - 2.9 Å of the Fourier transforms. The two simple diffusion paths Mn–O and Mn–Mn, as well as the first multiple one (Mn–O–O), were taken into account. Including the latter improves the quality of the fit, although its weighted contribution to the amplitude of the oscillations remains weak. The normalized $k^2\,\chi(k)$ experimental and fitted spectra are shown in figure 15, and the local structure parameters deduced from quantitative analysis are listed in Table 2. The experimental spectra of the λ-MnO_2 and $LiMn_2O_4$ standards were simulated to check the validity of both the analysis procedure and the used phases and amplitudes calculated from the FEFF code [31].

The results show that samples C and D are structurally very similar. They are octahedrally coordinated by oxygen. The Mn–O and Mn–Mn distances are consistent with those usually found in tetravalent manganese oxides such as β-MnO_2 (rutile-type structure, d_{Mn-O} = 1.88 + 1.90 Å) or λ-MnO_2 (delithiated spinel, d_{Mn-O} = 1.90 Å).

The insertion of lithium introduces very little change regarding the first coordination shell. However, the disorder at longer range is considerably increased, as shown by the uncertainties on Mn–Mn distances and coordination number (2nd shell) and the much higher value of σ^2 (see table 2, last line).

Finally, it should be pointed out that the σ^2 value of the Mn-O path (characteristic of the distribution of Mn-O distances) is constant within errors for sample C before and after discharge (see table 2). Thus the discharged sample shows no evidence of splitting of the Mn-O distance as could be expected in the presence of a Jahn-Teller distortion of the Mn–O octahedra [43]. Mn^{3+} compounds such as Mn_2O_3, $LiMnO_2$ or $LaMnO_3$ are known to contain heavily distorted Mn–O octahedral sites due to the Jahn-Teller effect. The absence of such a distortion in discharged sample C can be attributed to the oxidation state in the lithiated sample used in EXAFS, which is 3.30. This value is probably not close enough to 3.0 to induce a static distortion. This situation is comparable to that of the well-known perovskite-

type $(R_{1-x}A_x)MnO_3$ series (R = rare earth, A = Ca, Sr), which undergo a phase transition from a low-temperature static Jahn-Teller distorted structure to another one with averaged Mn-O distances at high temperature, corresponding to an incoherent ('dynamic') Jahn-Teller effect [44]. The occurence of Jahn-Teller distortion in lithium intercalation host materials on cycling effect is considered as a major cause of poor reversibility [45]. The nanostructural character and the absence of significant static Jahn-Teller distortion in manganese oxi-iodide studied here are probably major causes of its superior cyclability at 3 V compared to crystallized compounds such as $LiMn_2O_4$ or $LiMnO_2$.

Conclusions

The redox reaction of permanganate with iodide in aqueous medium at room temperature yields new X-ray amorphous manganese oxides with manganese oxidation state close to +4. These materials has been thoroughly characterized by chemical analysis, scanning and transmission electron microscopy, showing that they contains nanocrystalline crystallites of size 5-10- nm. These crystallites are agglomerated in blocks in the 10 μm range. From electron diffraction and X-ray absorption evidence, we conclude that these materials have a local structure typical of octahedrally coordinated Mn^{4+}. The initial capacity as a 3V cathode material in lithium batteries is high (ca. 180 mAh/g) and decreases slowly. We showed that a critical parameter in the electrochemical performances is a good electronic access to the cathode grains, depending critically on the quality of the oxide-carbon mixing. We studied two procedures to optimize this mixing at the smallest possible scale: (i) via extended grinding of the oxide prior to mixing with carbon, (ii) via an intimately mixed oxide-carbon composite obtained by incorporating conductive carbon in the reaction medium at the synthesis step. The latter route had been extensively studied before on $LiFePO_4$ cathodes (in which case it is even more critical because of the highly insulating character of this phosphate), and we confirm here the efficiency of oxide-carbon composites obtained by mixing carbon at an early stage of the cathode preparation. This procedure, however, is applicable only to preparation routes involving solutions, such as precipitation or sol-gel methods. The variations of capacities and capacity retention observed show that the actual cycling performances are in most cases limited by physico-chemical parameters such as grain size and distribution, porosity and quality of the oxide-conducting additive composite rather than by the intrinsic properties of the active material.

Acknowledgments

The authors wish to thank Yvonne Soldo for her assistance in EXAFS experiments.

References

1 H. Huang and P.G. Bruce, *J. Electrochem. Soc.* **1994**, *141*, L76.

2 W.P. Tang, X.J. Yang, Z.H. Liu and K. Ooi, *J. Mater. Chem.* **2003**, *13*, 2989.

3 H. Huang, S.C. Yin and L.F. Nazar, *Electrochem. Solid State Lett.* **2001**, *4*, A170.

4 P.P. Prosini, D. Zane AND M. Pasquali M, *Electrochimica Acta* **2001**, *46*, 3517.

5 S.H. Kang and J.B. Goodenough, *J. Electrochem. Soc.* **2000**, *147,* 3621.

6 S.H. Kang, J.B. Goodenough and L.K. Radenberg, *Chem. Mater.* **2001**, *13*, 1758.

7 J. Cho, G. Kim and H.S. Lim, *J. Electrochem. Soc.* **1999**, *146*, 3571.

8 N. Treuil, C. Labrugère, M. Ménétrier, J. Portier, G. Campet, A. Deshayes, S.J. Hwang, S.W. Song and J.H. Choy, *J. Phys. Chem.* **1999**, ***B103***, 2100.

9 B.B. Owens, S. Passerini and W.H. Smyrl, *Electrochimica Acta* **1999**, *45*, 215.

10 D. Larcher, C. Masquelier, D. Bonnin, Y. Chabre, V. Masson, J.B. Leriche and J.M. Tarascon, *J. Electrochem. Soc.* **2003**, *150*, A133.

11 S. Jouanneau, A. Le Gal-La Salle, A. Verbaere, M. Deschamps, S. Lascaud and D. Guyomard, *J. Mater. Chem.* **2003**, *13*, 921.

12 M. Nakayama, K. Watanabe, H. Ikuta, Y. Uchimoto and M. Wakihara, *Solid State Ionics* **2003**, *164*, 35.

13 S.H. Kang, J.B. Goodenough, L.K. Radenberg, *Electrochem. Solid State Lett.* **2001**, *4*, A49.

14 H.J. Choi, K.M. Lee, G.H. Kim and J.G. Lee, *J. Ceram Soc. Amer.* **2001**, *84*, 242.

15 D. Kovacheva, H. Gadjov, K. Petrov, S. Mandal, M.G. Lazarraga, L. Pascual, J.M. Amarilla, R.M. Rojas, P. Herrero and J.M. Rojo, *J. Mater. Chem.* **2002**, *12*, 1184.

16 V. Ganesh-Kumar, J.S. Gnanaraj, S. Ben-David, D.M. Pickup, E.R.H. Van Eck, A. Gedanken and D. Aurbach, *Chem. Mater.* **2003**, *15*, 4211.

17 O. Glemser and H. Meisiek, *Naturwiss.* **1957**, *44*, 614.

18 P. Loganathan and R.G. Burau, *Geochim. Cosmoschim. Acta* **1973**, *37*, 1277.

19 K.M. Parida, Kanungo SB, Sant BR, *Electrochimica Acta* **1981**, *26*, 435.

20 P. Strobel and J.C. Charenton, *Rev. Chim. Minérale* **1986**, *23*, 125

21 J. Kim and A. Manthiram, *Nature* **1997**, *390*, 265.

22 A. Ibarra-Palos, M. Anne, P. Strobel, *Solid State Ionics* **2001**, *138*, 203.

23 C.R. Horne, U. Bergmann, J. Kim, K.A. Striebel, A. Manthiram, S.P. Cramer and E.J. Cairns, *J. Electrochem. Soc.* **2000**, *147,* 395.

24 A. Ibarra-Palos, P. Strobel, O. Proux, J.L. Hazemann, M. Anne, M. Morcrette, *Electrochimica Acta* **2002**, *47*, 3171.

25 S. Kobayashi, I.R.M. Kottegoda, Y. Uchimoto and M. Wakihara, *J. Mater. Chem.* **2004**, *14*, 1843

26 S.J. Hwang, H.S. Park, J.H. Choy and G. Campet, *J. Phys. Chem. B* **2001,** *105*, 335 and **2002,** *106*, 4053.

27 A. Ibarra-Palos, P. Strobel, C. Darie, M. Bacia and J.B. Soupart, *J. Power Sources* **2005** *146*, 294.

28 A.H. Thompson, *J. Electrochem. Soc.* **1979**, *126*, 608.

29 O. Proux, X. Biquard, E. Lahera, J.-J. Menthonnex, A. Prat, O. Ulrich, Y. Soldo, P. Trévisson, G. Kapoujvan, G. Perroux, P. Taunier, D. Grand, P. Jeantet, M. Deleglise, J.-P. Roux and J.-L. Hazemann, *Physica Scripta* **2005,** *115*, 970.

30 F. Le Cras, D. Bloch and P. Strobel, *J. Power Sources* **1996**, *63*, 71.

31 B. Ravel and M. Newville *Physica Scripta* **2005,** *115*, 1007.

32 S.J. Hwang, C.W. Kwon, G. Campet and J.H. Choy, *Electrochem. Solid State Lett.* **2001**, *4*, A49.

33 R.G. Burns, V.M. Burns and H.W. Stockman, *Amer. Mineral.* **1983**, *68*, 972.

34 J. Kim and A. Manthiram, *Electrochem. Solid State Lett.* **1999**, *2*, 55.

35 J.J. Xu, G. Jain and J. Yang, *Electrochem. Solid State Lett.* **2002**, **5**, A152.

36 P. Strobel and C. Mouget, *Mater. Res. Bull.* **1999**, *28*, 93.

37 C.J. Chen and M.S. Whittingham, *J. Electrochem. Soc.* **1997**, *144*, L64.

38 R. Dominko, M. Gaberscek, J. Drofenik, M. Bele and J. Jamnik, *Electrochim. Acta* **2003**, *48*, 3709.

39 S.J. Hwang, C.W. Kwon, G. Campet and J.H. Choy, *Electrochem. Solid State Lett.* **2004**, *7*, A49

40 M. Morcrette, P. Barboux, J. Perrière, T. Brousse, A. Traverse, J.P. Boilot, *Solid State Ionics* **2001**, *138*, 213.

41 M. Belli, A. Scafati, A. Bianconi, S. Mobilio, L. Palladino, A. Reale, E. Burattini, *Solid State Comm*. **1980**, *35*, 355.

42 A. Manceau, A.I. Gorshkov, V.A. Drits, *Amer. Mineral.* **1992**, *77*, 1133.

43 A. Paolone, C. Castellano, R. Cantelli, G. Rousse and C. Masquelier, *Phys. Rev. B* **2003**, *68*, 014108

44 P.G. Radaelli, M. Marezio, H.Y. Hwang, S.W. Cheong, B. Batlogg, *Phys. Rev. B* **1996**, *54*, 8992.

45 M.M. Thackeray, *J. Electrochem. Soc.* **1995**, *142*, 2558.

Table I. Syntheses conditions and product analysis

Sample	Reaction medium		Product composition			
	Li/Mn in solution	carbon added	Na/Mn (molar)	Li/Mn (molar)	C/Mn (molar)	I/Mn [1]
A	≈ 6	no	0.22	0.38	-	1
B	≈ 6	yes	0.07	0.46	1.66	2
C	10.6	no	0.06	0.53	-	4
D	10.4	yes	0.08	0.55	1.74	4

[1] *approximate EDX analysis on powder samples*

Table 2. Local structure parameters deduced from quantitative analysis of EXAFS data. R = interatomic distance, CN = coordination number, σ = Debye-Weller factor (ΔE values not included because they were found constant within error bars in all simulations).

sample	X-Y pair	R (Å)	CN	σ^2 (Å^2)	R-factor
λ-MnO_2 standard	Mn - O	1.882 (11)	5.5 (1.2)	0.0019	0.019
	Mn - Mn	2.880 (15)	5.7 (0.7)	0.0054	
$LiMn_2O_4$ standard	Mn - O	1.894 (7)	5.8 (0.9)	0.0038	0.008
	Mn - Mn	2.891 (7)	6.1 (0.7)	0.0054	
C	Mn - O	1.878 (11)	5.9 (1.2)	0.0038	0.021
	Mn - Mn	2.862 (13)	3.8 (1.0)	0.0056	
D	Mn - O	1.880 (9)	6.5 (1.1)	0.0039	0.018
	Mn - Mn	2.860 (10)	4.4 (0.9)	0.0056	
C after discharge	Mn - O	1.889 (12)	5.4 (1.1)	0.0037	0.018
	Mn - Mn	2.90 (2)	5.2 (2.6)	0.013	

FIGURE CAPTIONS

Figure 1. XRD diagrams of samples A to D (Cu Kα radiation). Top : standard (normally crystallized) manganese carbonate with same acquisition conditions. The broad bump around 19° is due to the adhesive tape used as sample holder in transmission geometry.

Figure 2. SEM micrographs of samples C and D (initial magnification 175x). The figures are labelled "C" and "D" with grinding time in minutes (0, 15 or 60).

Figure 3. SEM micrographs of samples A and B (initial magnification 2000x). The figures are labelled "A" and "B" with grinding time in minutes (0 or 60).

Figure 4. Transmission electron micrographs of samples A and D (as marked) at different magnifications.

Figure 5. Selected area electron diffraction pattern of a crystallite from sample D.

Figure 6. Step-potential electrochemical spectroscopy of sample D recorded at 10 mV/30 mn scan rate. Inset: evolution of the incremental current across the reduction peak.

Figure 7. First galvanostatic discharge-charge cycle of samples A to D. Conditions : room temperature, voltage window 1.8-3.8 V, discharge regime C/18-C/20 (for 1 Li/Mn).

Figure 8. Comparing the first discharge-charge cyclings of samples A-D before and after grinding (same conditions as in fig.1). (a) carbon mixed after synthesis, (b) carbon added at the synthesis stage. The arrows show the evolution from pristine to ground samples.

Figure 9. Evolution of capacity of samples C (top) and D (bottom) as a function of cycling for different grinding times. Cycling conditions are as in Fig. 7.

Figure 10. Evolution of cycling capacities at the first (d1), third (d3) and thirtiest (d30) discharge as a function of grinding time. Full lines: sample C (carbon mixed after preparation), dashed lines: sample D (carbon included in synthesis stage).

Figure 11. Evolution of capacity of optimized samples C (with 60 mn grinding) and D (not ground) at C/20 in potential window 1.8-3.8 V.

Figure 12. Comparing the discharge capacities at first (Q1), third (Q3) and thirtiest (Q30) cycle for optimized samples A-C (top) and B-D (bottom).

Figure 13. XANES spectra of samples C and D, and of sample C after discharge corresponding to the insertion of 0.6 Li. Spectra of standards λ-MnO_2, $LiMn_2O_4$ and Mn_2O_3 (dashed lines) are included for comparison.

Figure 14. Evolution of the energies of edge maximum (left) and of first inflexion point (right) as a function of manganese valence. Triangles : standards (as in Fig.12), circles : nanocrystalline samples.

Figure 15. Normalized $k^2\chi(k)$ for different samples studied in EXAFS. Open symbols : experimental data; solid lines : fitted spectra.

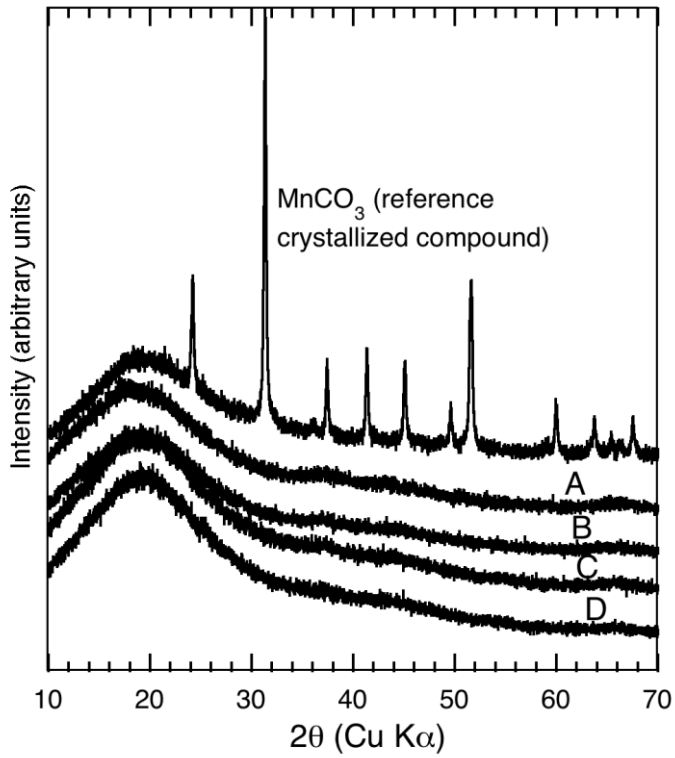

Figure 1. XRD diagrams of samples A to D (Cu Kα radiation). Top : standard manganese carbonate with same acquisition conditions. The broad bump around 19° is due to the adhesive tape used as sample holder in transmission geometry.

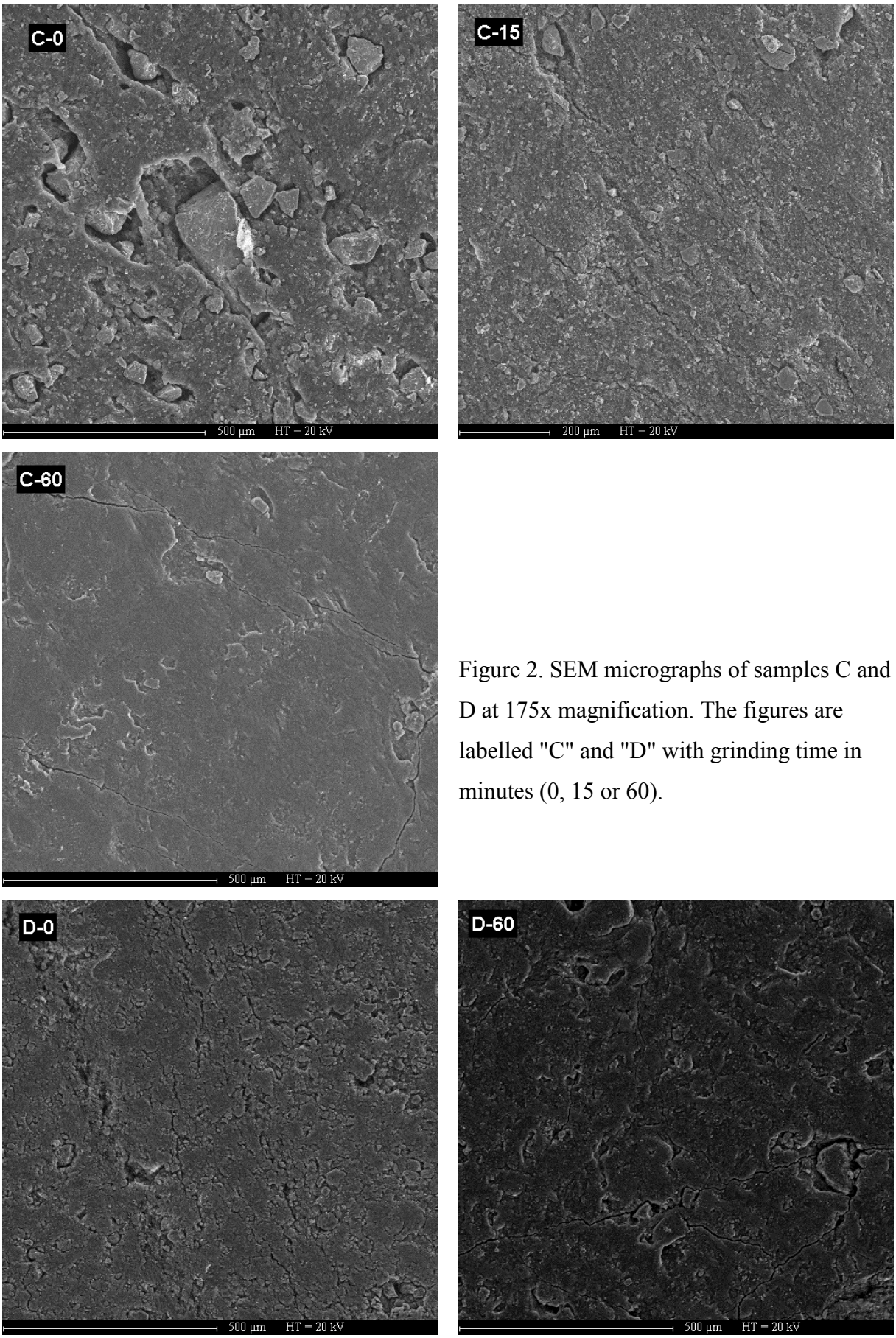

Figure 2. SEM micrographs of samples C and D at 175x magnification. The figures are labelled "C" and "D" with grinding time in minutes (0, 15 or 60).

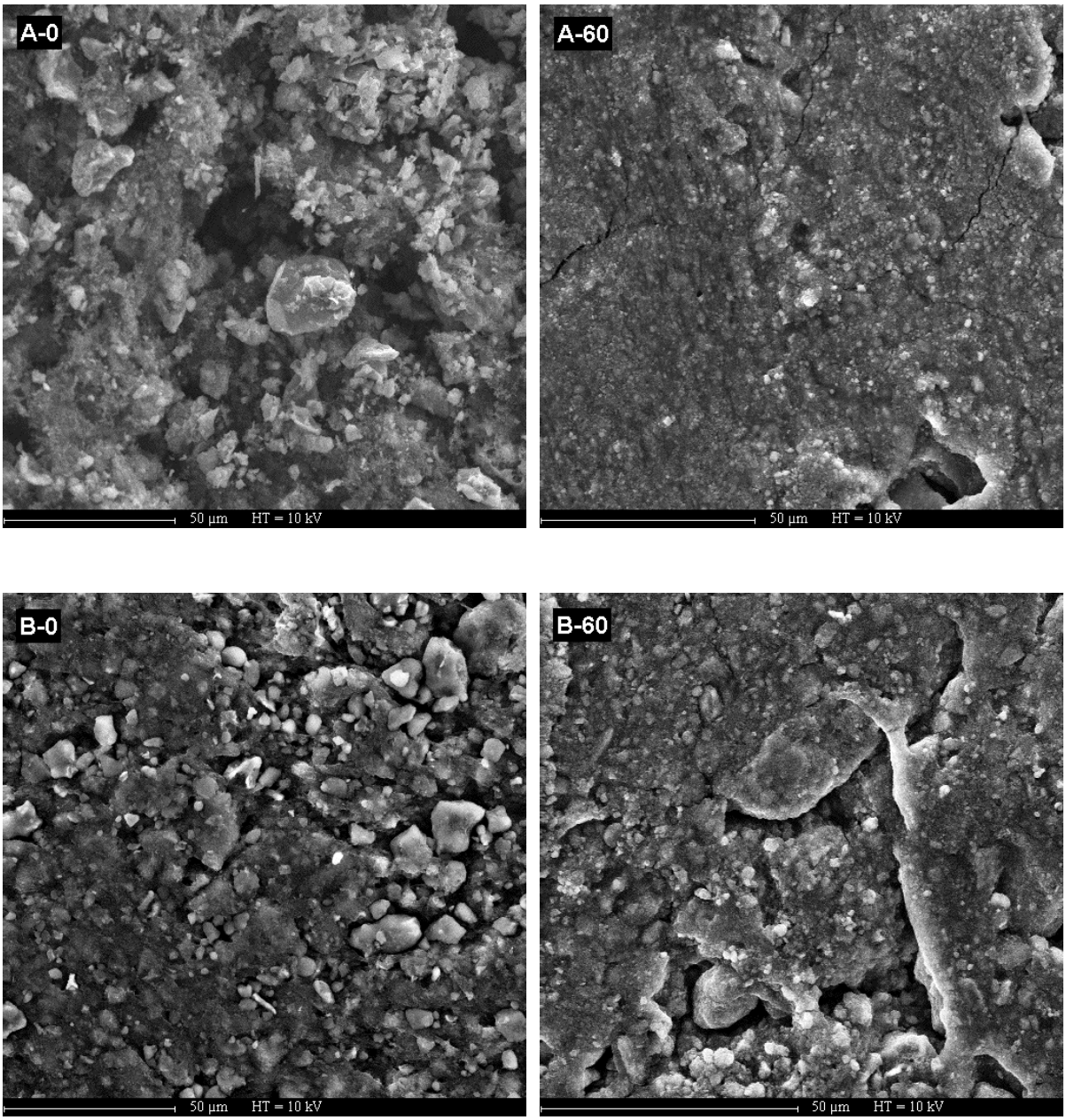

Figure 3. SEM micrographs of samples A and B at 2000x magnification. The figures are labelled "A" and "B" with grinding time in minutes (0 or 60).

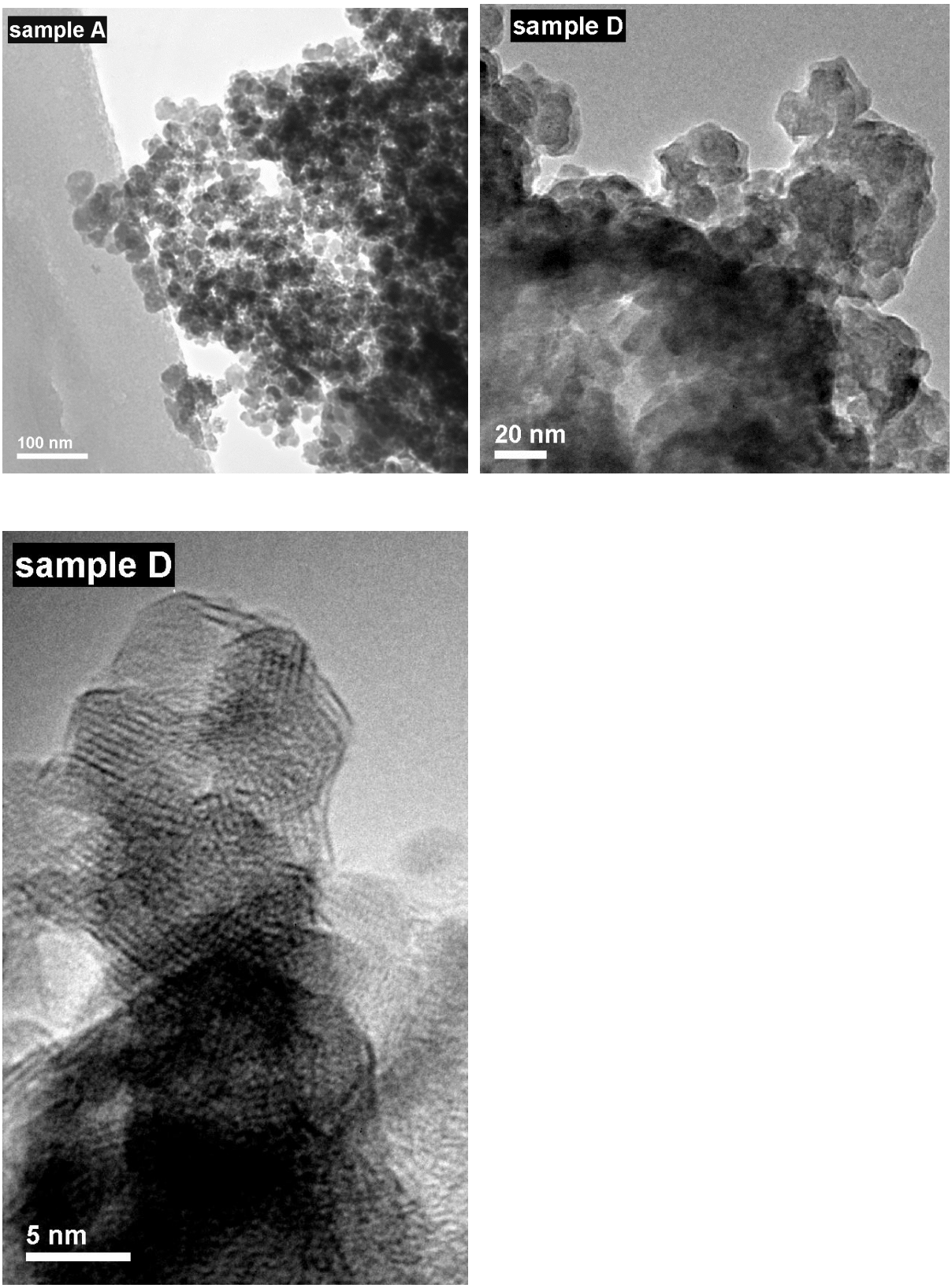

Figure 4. Electron diffraction micrographs of samples A and D (as marked) at different magnifications.

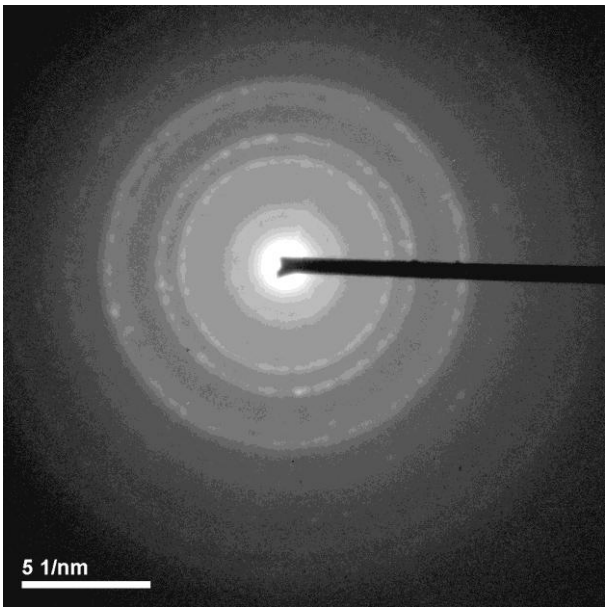

Figure 5. Selected area electron diffraction pattern of a crystallite from sample D.

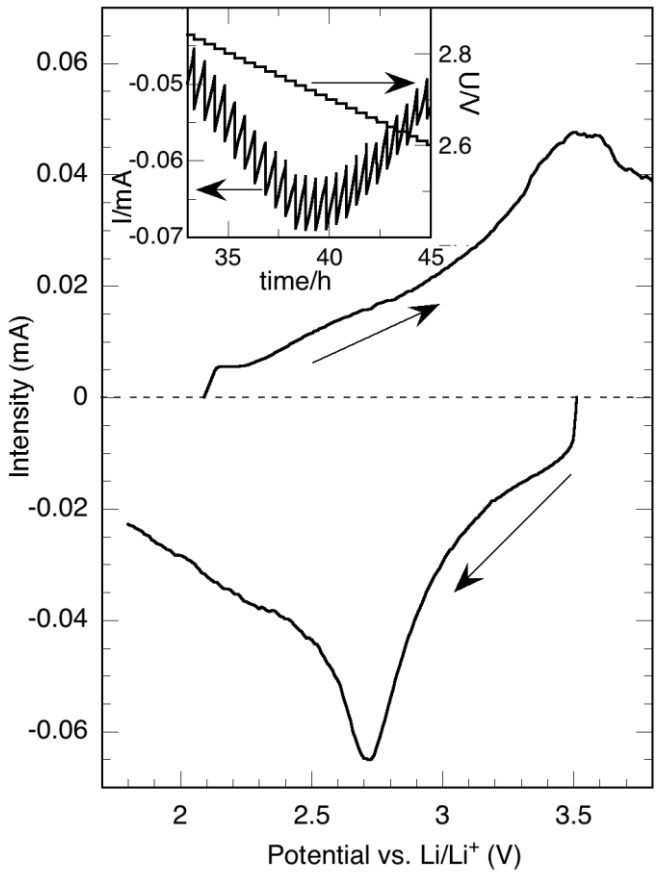

Figure 6. Step-potential electrochemical spectroscopy of sample D recorded at 10 mV/30 mn scan rate. Inset: evolution of the incremental current across the reduction peak.

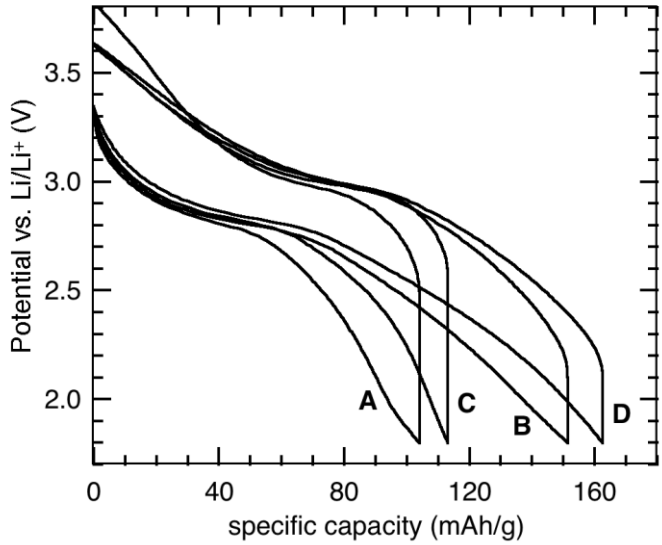

Figure 7. First galvanostatic discharge-charge cycle of samples A to D. Conditions : room temperature, voltage window 1.8-3.8 V, discharge regime C/18-C/20 (for 1 Li/Mn).

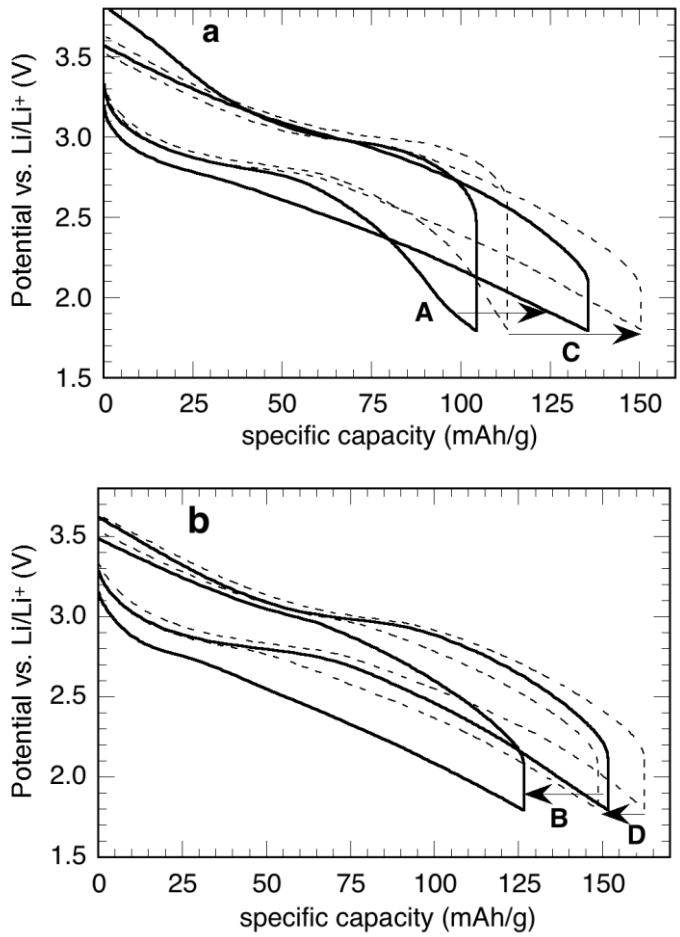

Figure 8. Comparing the first discharge-charge cyclings of samples A-D before and after grinding (same conditions as in fig.1). (a) carbon mixed after synthesis, (b) carbon added at the synthesis stage. The arrows show the evolution from pristine to ground samples.

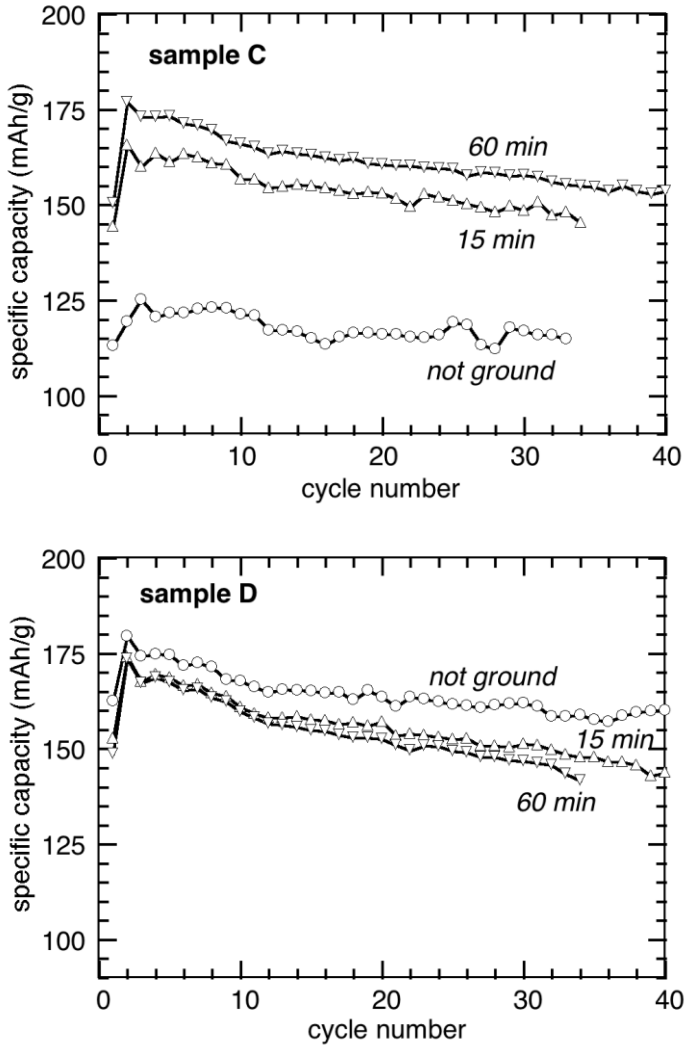

Figure 9. Evolution of capacity of samples C (top) and D (bottom) as a function of cycling for different grinding times. Cycling conditions are as in Fig. 7.

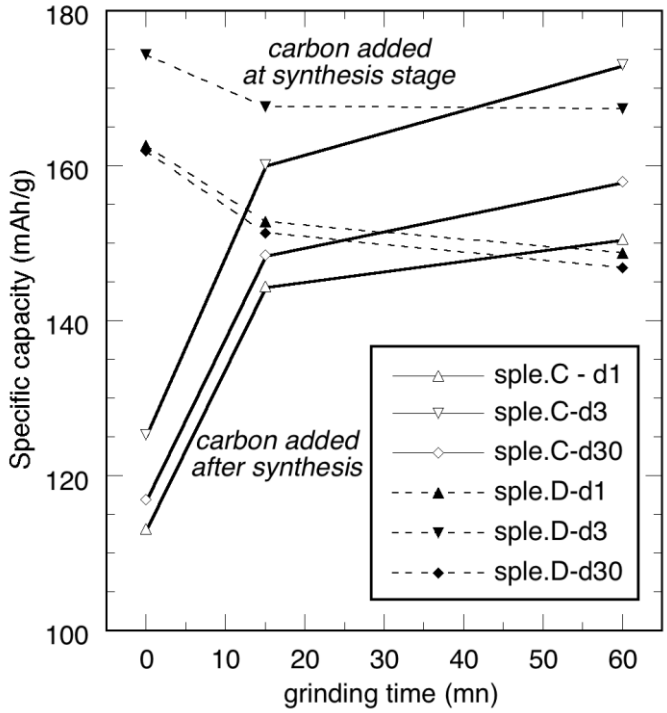

Figure 10. Evolution of cycling capacities at the first (d1), tenth (d10) and thirtiest (d30) discharge as a function of grinding time. Full lines: sample C (carbon mixed after preparation), dashed lines: sample D (carbon included in synthesis stage).

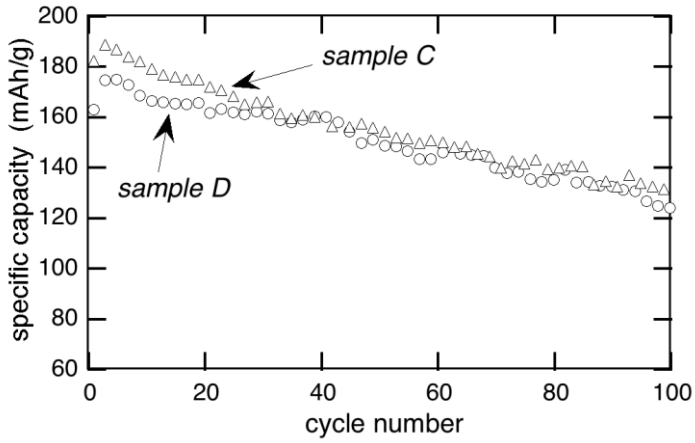

Figure 11. Evolution of capacity of optimized samples C (with 60 mn grinding) and D (not ground) at C/20 in potential window 1.8-3.8 V.

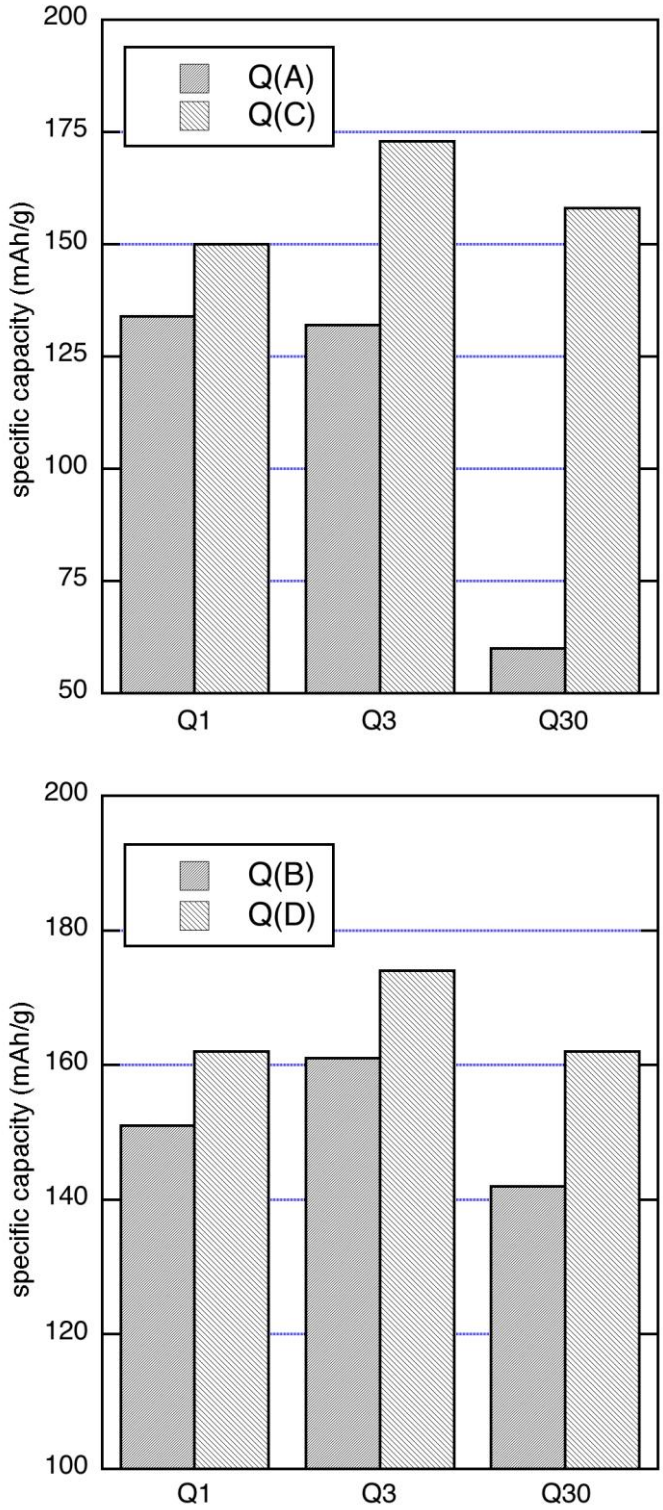

Figure 12. Comparing the discharge capacities at first (Q1), tenth (Q10) and thirtiest (Q30) cycle for optimized samples A-C (top) and B-D (bottom).

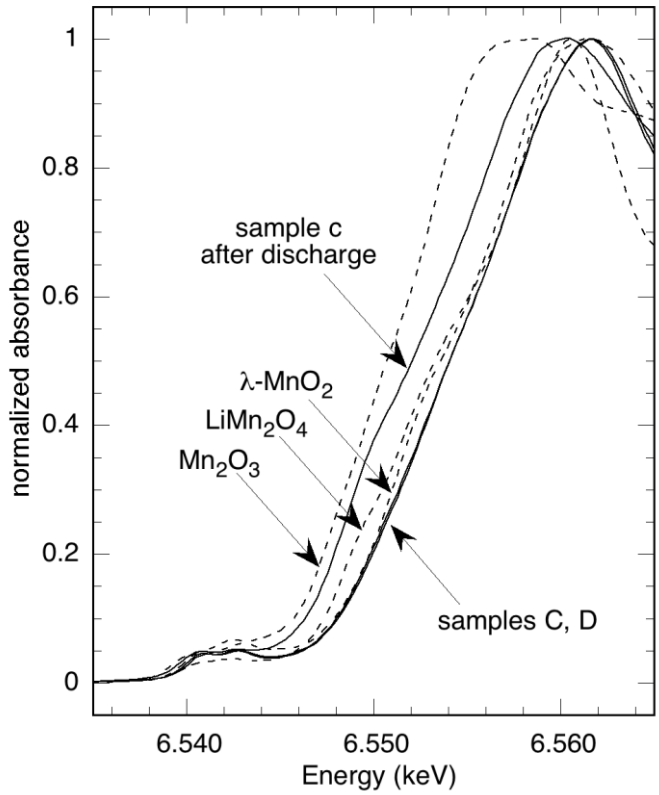

Figure 13. XANES spectra of samples C and D, and of sample C after discharge corresponding to the insertion of 0.6 Li. Spectra of standards λ-MnO_2, $LiMn_2O_4$ and Mn_2O_3 are included for comparison.

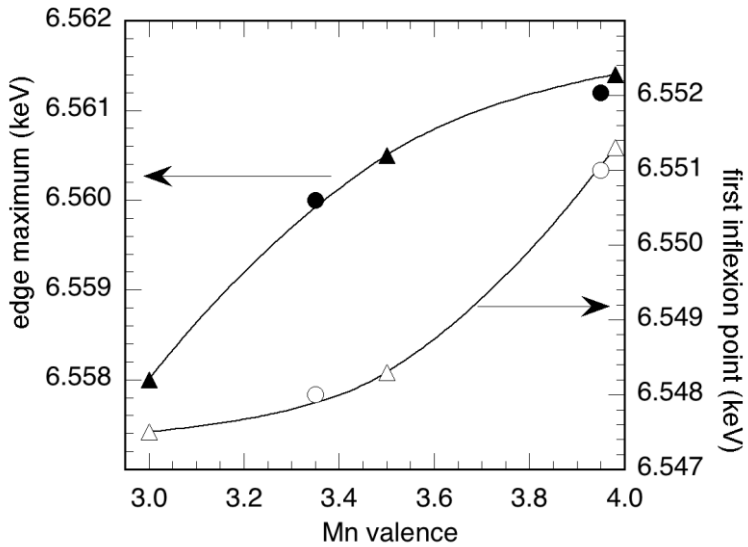

Figure 14. Evolution of the energies of edge maximum (left) and of first inflexion point (right) as a function of manganese valence. Triangles : standards (as in Fig.12), circles : nanocrystalline samples.

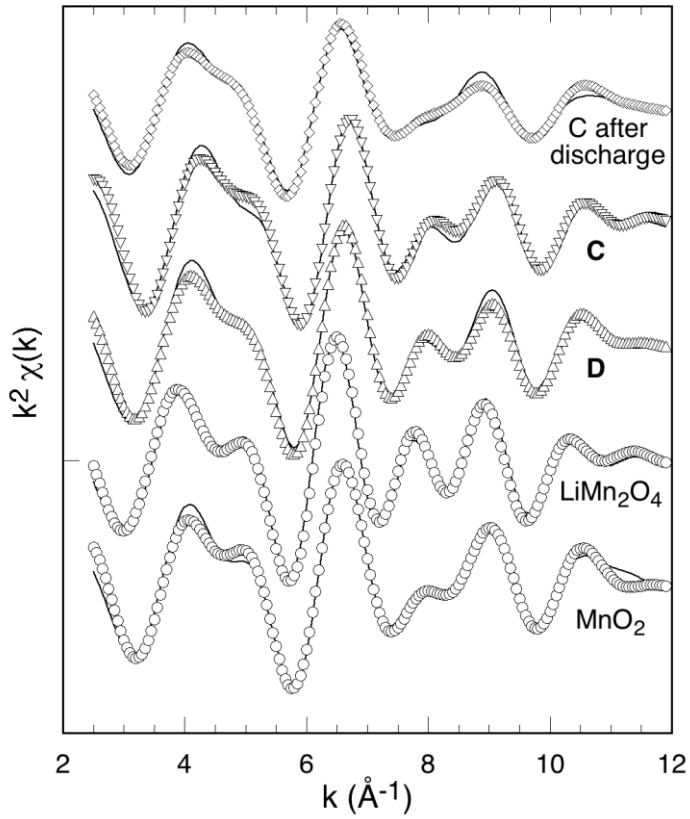

Figure 15. Normalized $k^2\chi(k)$ for different samples studied in EXAFS. Open symbols : experimental data; solid lines : fitted spectra.